

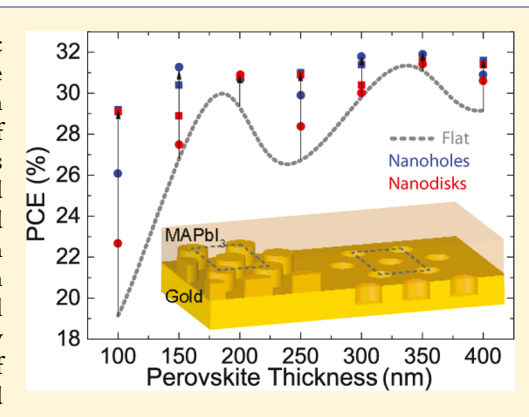
Plasmon-Enhanced Thin-Film Perovskite Solar Cells

Tianyi Shen, Stylianos Siontas, and Domenico Pacifici*

School of Engineering, Brown University, 184 Hope Street, Providence, Rhode Island 02912, United States

Supporting Information

ABSTRACT: We report on plasmon-enhanced hybrid organic-inorganic perovskite solar cells with methylammonium lead iodide (MAPbI₃) as the active absorbing material. Three-dimensional finite-difference time-domain simulations were performed on perovskite solar cells that consist of perovskite films with varied thicknesses on top of corrugated gold electrodes with different light trapping geometries, such as arrays of nanoholes and nanodisks. The absorption within the perovskite and gold films was estimated by calculating the electric field at every mesh point within the simulation volume, which allowed for the calculation of the solar cell power conversion efficiency (PCE) as a function of relevant design parameters. Optimal nanostructure designs were obtained by systematically varying the geometry dimensions. The results show that 100 nm-thick perovskite films on top of corrugated gold electrodes can exhibit up to 52% increase in PCE compared to their flat counterparts (i.e., from 19.2% for a flat cell to 29.2% for an



optimized nanocorrugated cell). Moreover, we show that a 150 nm-thick perovskite film cell with opportunely corrugated back metal contacts can exhibit a PCE value of 31.3%, which is comparable to that of a 400 nm-thick bulk-like cell (31.6%). These findings may pave the way for plasmon-enhanced high-performance perovskite solar cells with ultrathin absorbing layers.

INTRODUCTION

Hybrid organic-inorganic perovskite solar cells have proven to be the most rapidly growing photovoltaic technology to date with reported power conversion efficiency (PCE) reaching up to 23.2%. The high PCE, together with low-cost fabrication processes²⁻⁶ and remarkable optoelectronic properties, such as high absorption coefficient⁸ and long carrier diffusion length,9 makes perovskite solar cells a promising alternative to traditional silicon solar cells. Perovskite materials can be described by the general formula ABX3, where A is an organic cation [e.g., methylammonium CH₃NH₃ (MA) or formamidinium $HC(NH_2)_2$, B is an inorganic cation [e.g., most commonly lead (Pb)], and X is a halide which is usually iodine (I). So far, the most widely used perovskite material has been methylammonium lead iodide CH₃NH₃PbI₃ (MAPbI₃) which possesses an optical energy band gap of 1.55 eV, 10 close to the ideal value of 1.34 eV for single junction solar cells as imposed by the Shockley-Queisser limit. 11,12 By adding a fraction of Sn, Br, or Cl, the band gap of MAPbI3 can be tuned from 1.3 to 2.3 eV, 13-16 which allows for the design of multijunction cells with absorption properties that are better tuned to the solar spectrum. Although the absorption coefficient of MAPbI₃ is so high that thin (~300-400 nm) layers of the material are sufficient to absorb most of the incident visible solar spectrum, the reported efficiency of these perovskite solar cells is still lower than the theoretical limit. Among other methods, plasmonic absorption enhancement has been extensively utilized to improve the performance of various solar cell technologies, 17,18 including organic, 19,20 dye-Similarly, the sensitized,²¹ and semiconductor materials.²

performance of perovskite solar cells can also be enhanced by employing nanoparticles (either dielectric^{26,27} or metallic²⁸⁻³⁴) or plasmonic concentrators that are embedded in the cell electrodes^{35–38} and can enhance the optical field intensity within the active layer.

The main aim of this paper is to investigate the feasibility of plasmon-enhanced perovskite solar cells with significantly thinner active layers to achieve similar performance compared to thicker cells, which can bring the following benefits: (a) because most high-performance perovskite cells use thick Pbbased materials, which may pose threats to human health and the environment, drastically reducing the thickness of the active layer would allow for a significant suppression of the overall amount of toxic material employed to fabricate the cell; 28 (b) moreover, cells with thinner active layers but with the same overall light absorption are characterized by higher carrier concentration and therefore higher open circuit voltage and efficiency compared to thicker cells;³⁹ and (c) finally, thinner films are more amenable to fabricate flexible solar cells.40

Here, we present a systematic study of the plasmonic absorption enhancement in MAPbI3 perovskite solar cells using three-dimensional finite-difference time-domain (FDTD) simulations. Specifically, the PCE enhancement was calculated using the simulated electric fields within perovskite films coated on top of flat or corrugated gold surfaces [i.e.,

Received: July 23, 2018 Revised: September 13, 2018 Published: September 19, 2018 The Journal of Physical Chemistry C

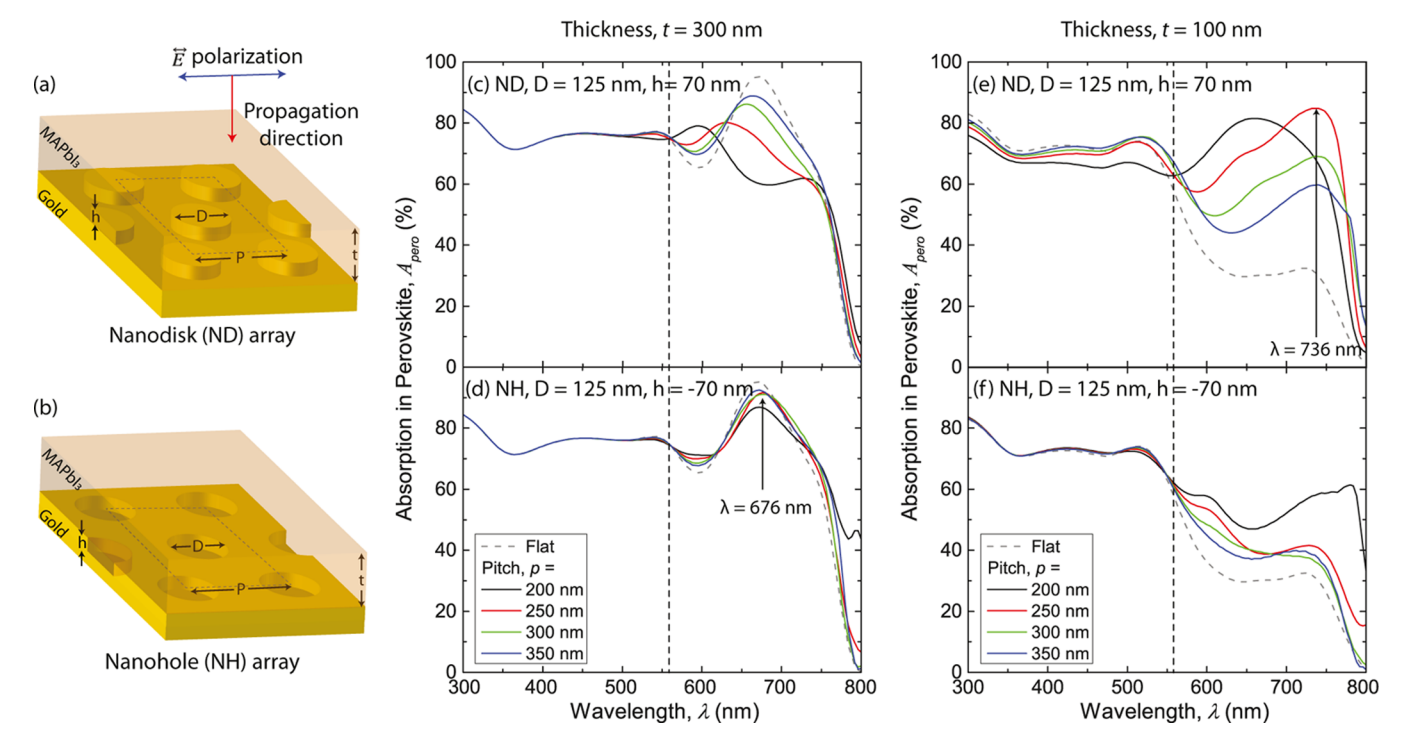


Figure 1. (a,b) Schematic of simulated perovskite/gold geometries consisting of a perovskite (MAPbI₃) thin film on top of corrugated gold surfaces with a ND or NH array arranged in a hexagonal pattern. D and h denote the diameter and height for the NDs or NHs, respectively; p represents the pitch of the hexagonal lattice; t is the perovskite film thickness. The gold layer thickness is assumed to be semi-infinite. (c-f) Simulated absorption spectra in the perovskite film of thicknesses t = 100 and 300 nm for flat (dashed gray lines) and corrugated gold substrates (solid lines) with ND/NH diameter D = 125 nm and height $h = \pm 70$ nm. The pitch of the hexagonal pattern p = 200-350 nm. The vertical dashed line indicates $\lambda = 560$ nm, below which the transmitted light through the perovskite film is negligible due to the large imaginary part of its refractive index.

nanodisk (ND) or nanohole (NH) arrays] by leveraging various geometry parameters (i.e., perovskite film thickness t, ND and NH diameter D and height h, as well as array pitch p).

COMPUTATIONAL DETAILS

A commercial-grade simulator (FDTD Solutions by Lumerical Inc.) based on the FDTD method was used to perform all calculations reported in this paper. 41 The simulated structure is a simplified perovskite solar cell without an electron or hole transporting layer, nor a top transparent contact. It consists only of a MAPbI3 absorbing film and a flat or corrugated gold electrode with NDs or NHs in a hexagonal pattern, as shown in Figure 1a,b with the unit cell denoted by dashed lines. A positive value of h corresponds to ND arrays while a negative h corresponds to NH arrays on top of the gold contact. The top surface of the perovskite layer is set to be flat, in accordance to experimentally realistic perovskite films typically fabricated via spin coating. A plane wave light source with wavelength λ = 300-800 nm was positioned above the cell stack. Perfectly matched layers were used at the top and bottom boundaries. In contrast, anti-symmetric and symmetric boundary conditions were used in the lateral directions because of the periodicity of the structure. The mesh size was set to 1 nm in Cartesian coordinates, which balanced the accuracy and computational cost. The real and imaginary parts of the refractive index used in the simulation were obtained by fitting the experimental tabulated data for MAPbI₃⁴² and gold⁴³ (see Supporting Information). Simulations were performed for various values of relevant geometry parameters, such as perovskite film thickness t, ND/NH diameter D and height h, and array pitch p, as shown in Figure 1a,b. The electric field \vec{E} was obtained at each

mesh point within the simulation volume, which allows for the decoupling of the absorption A in the perovskite and gold films, respectively, by using the following equation

$$A(\lambda) = \int \frac{\pi c}{\lambda} \varepsilon''(\lambda) |\vec{E}(\lambda)|^2 dV$$
 (1)

where c is the speed of light, $e''(\lambda)$ is the wavelength-dependent imaginary part of the permittivity, and \vec{E} is the electric field. The integration in eq 1 over the total volume V of the perovskite or gold results in the absorption within that specific material.

■ RESULTS AND DISCUSSION

Figure 1c-f presents the simulated absorption spectra $A_{pero}(\lambda)$ within the perovskite film with representative thicknesses [i.e., t = 300 (c,d) and 100 nm (e,f)] on top of flat and corrugated (ND or NH arrays) gold surfaces. The nanostructure geometry is fixed with D = 125 nm and $h = \pm 70$ nm, while p varies from 200 to 350 nm with incremental steps of 50 nm. For t = 300nm (see Figure 1c,d) and λ < 560 nm (as denoted by vertical dashed lines), the absorption is almost independent of the geometric parameters because of the high absorption coefficient of MAPbI3 in that wavelength range (see Supporting Information). The spectral shapes in this wavelength range are attributed to the wavelength-dependent transmission at the air/perovskite interface. For $\lambda > 560$ nm, the Fabry-Pérot cavity modes can significantly affect the absorption in MAPbI₃. For flat (uncorrugated) metal substrates, the observed spectral peaks correspond to destructive interference (low reflection, high absorption), whereas the dips correspond to constructive interference The Journal of Physical Chemistry C

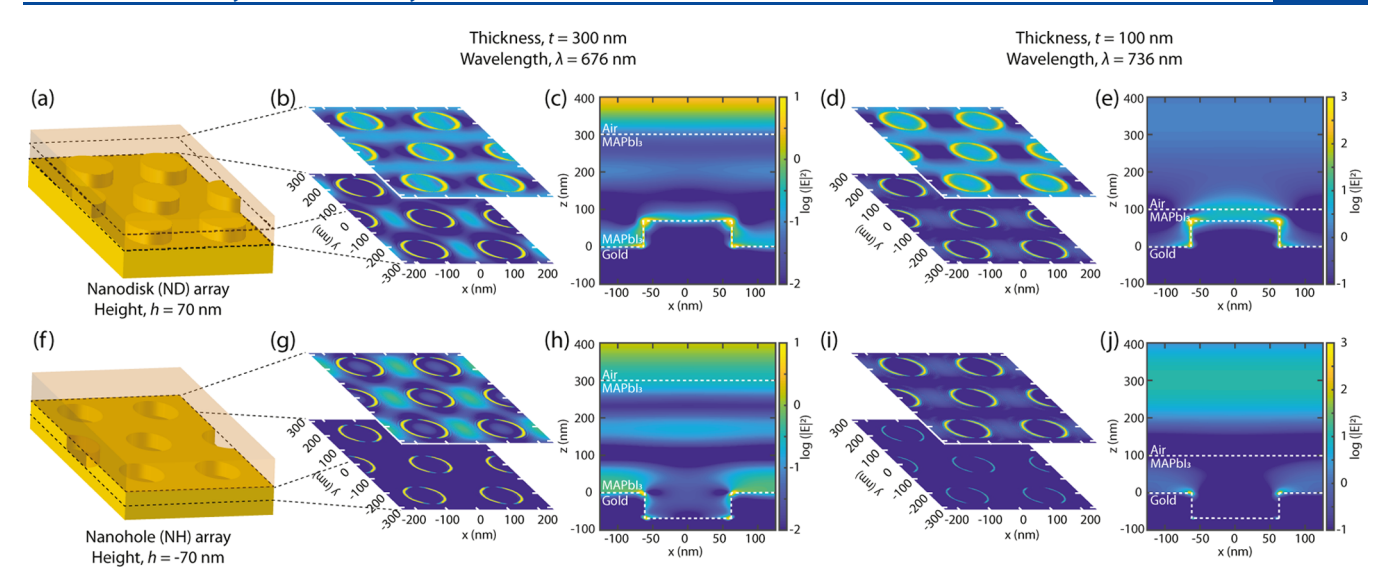


Figure 2. (a–e) ND and (f–j) NH array schematic and electric field intensity profiles $|\vec{E}|^2$ at the horizontal (i.e., both top and bottom interfaces of nanostructures) and vertical cross sections for t = 300 nm and $\lambda = 676$ nm as well as t = 100 nm and $\lambda = 736$ nm. The nanostructure geometry is $h = \pm 70$ nm, D = 125 nm, and p = 250 nm.

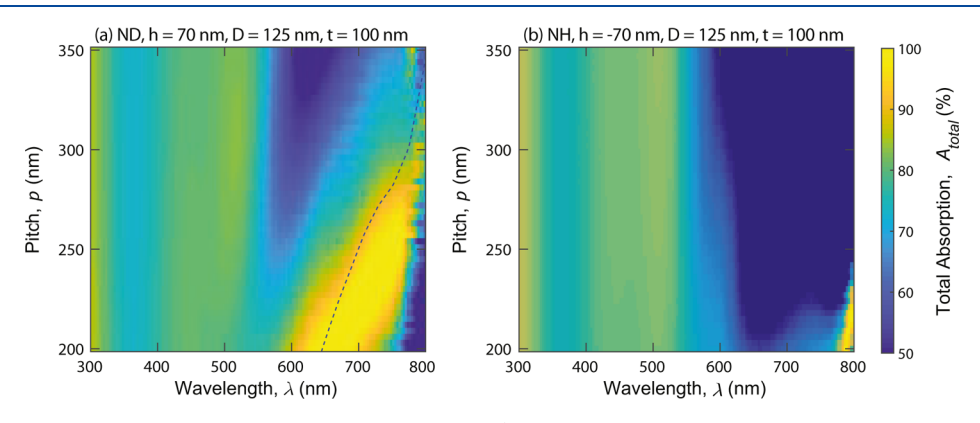


Figure 3. Representative color maps of simulated total absorption spectra (including contributions from both perovskite film and gold substrate) as a function of the incident light wavelength λ and array pitch p for (a) ND arrays and (b) NH arrays. The nanostructure diameter D=125 nm, its height $h=\pm70$ nm, and the perovskite thickness t=100 nm. The dashed line in (a) represents the collective SPP resonance mode indicated in eq 2, which agrees well with the wavelength positions of the FDTD-simulated absorption peaks.

(high reflection, low absorption). In the presence of nanostructured gold substrates, the absorption in the perovskite film is enhanced at wavelengths near the constructive interference wavelength (λ = 598 nm) because of plasmonic effects. On the contrary, compared to the flat case, the absorption of incident light with wavelength near the destructive interference wavelength (λ = 670 nm) is systematically suppressed with decreasing array pitches in the presence of nanostructured metal contacts. This effect is attributed to the disruption of the Fabry–Pérot cavity modes caused by significant light scattering by the nanostructures (NDs or NHs), with the NDs being more effective due to their higher scattering cross section.

When the thickness t is decreased to 100 nm (see Figure 1e,f), the perovskite film no longer supports Fabry–Pérot cavity modes. Moreover, the film is less effective at absorbing incident light in a single pass, and, as a result, plasmonic effects can play a more significant role. For $\lambda < 560$ nm (as denoted by vertical dashed lines), the spectral shape is still mainly determined by the wavelength-dependent reflection at the air/perovskite interface. In the presence of NDs (see Figure 1e), the absorption in the perovskite film is reduced compared to the flat case and is shown to decrease with decreasing array

pitch. This results from the fact that the metal disks occupy space at the expense of perovskite material. Structures with smaller array pitch are characterized by a higher density of NDs, which determines an overall reduction in perovskite material and a concomitant reduction in light absorption. For $\lambda > 560$ nm, the incident light is not entirely absorbed by MAPbI₃ and a significant fraction can reach the perovskite/metal interface thus strongly interacting with the gold nanostructures. Specifically, for both types of structures (i.e., NDs and NHs), the absorption in a 100 nm-thick film on top of corrugated films is much higher compared to the flat case because of plasmonic effects.

It is worth noting that for t=100 nm, NHs determine an overall smaller absorption compared to NDs (see Figure 1e,f), although the absorption enhancement can be significantly higher especially near the band edge. For t=300 nm, the NH geometry can help achieve overall higher absorption values compared to ND arrays (see Figure 1c,d). Moreover, the NH arrays seem to better preserve the Fabry–Pérot cavity modes, therefore in this case the solar cell absorption can benefit from both plasmon resonances and Fabry–Pérot cavity modes.

The Journal of Physical Chemistry C

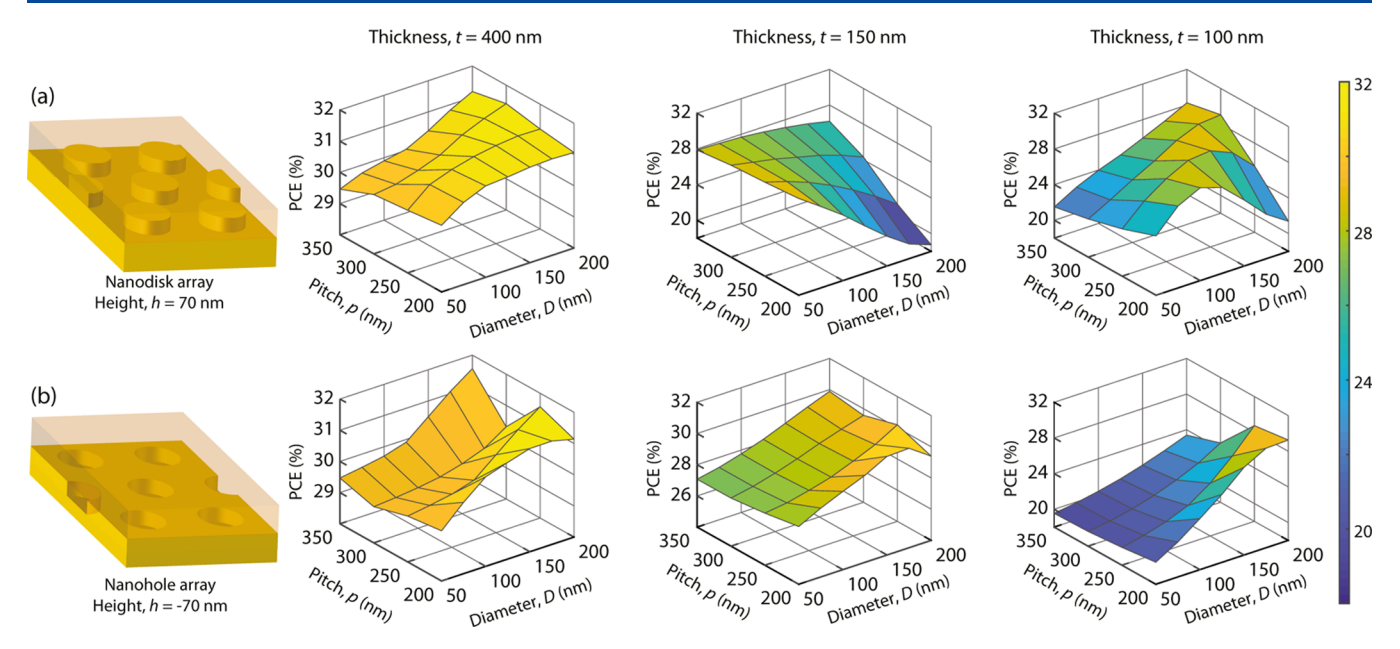


Figure 4. Examples of calculated PCE as a function of pitch and diameter for representative perovskite thickness values, t = 400, 150, and 100 nm with (a) NDs or (b) NHs patterns etched in the back metal contact. The height of the nanostructures $h = \pm 70$ nm. Left panels report schematics of both ND and NH structures.

To better understand the physical mechanisms responsible for enhanced absorption, the electric field intensity distribution $|\dot{E}|^2$ for both types of nanostructures is calculated and presented in Figure 2 at a wavelength corresponding to the absorption peaks. The two horizontal cross sections in Figure 2b,d,g,i correspond to the top and bottom planes of the nanostructures, while the vertical cross sections through the center of the nanostructure show the field intensity across different layers in Figure 2c,e,h,j. For t = 300 nm and $\lambda = 676$ nm, bright horizontal bands in the perovskite layer (see Figure 2c,h) result from Fabry-Pérot cavity modes. Fabry-Pérot interference effects are weaker in the ND array compared to the NH array because of stronger scattering provided by the NDs. The features similar to bright rings on top and bottom of the nanostructure correspond to localized surface plasmon resonances with high field intensity. Even though localized plasmonic resonances are weaker in NH arrays, Fabry-Pérot cavity modes are better preserved and yield a relatively higher absorption when compared with ND arrays (see red lines in Figure 1c,d). In contrast, for t = 100 nm and $\lambda = 736$ nm, Fabry-Pérot cavity modes no longer exist (see Figure 2e,j). Instead, purely plasmonic effects become dominant in the absorbing process as observed by stronger localized fields at the ND/perovskite interface that lead to overall higher absorption in the perovskite films (see red lines in Figure 1e,f). It is worth noting that even though Figure 2 reports similar features corresponding to localized surface plasmon resonances for different perovskite film thicknesses, the actual field intensity is 2 orders of magnitude stronger for the 100 nm-thick film than for the 300 nm-thick film, as captured by the different logarithmic range of the corresponding color bar

Furthermore, here we investigate the physical origin of the red shift observed in the absorption peaks reported in Figure 1c with increasing array pitch. Simulated absorption intensity maps are shown in Figure 3a, which reports total absorption as a function of array pitch and incident wavelength. The presence of a high absorption band that red shifts with

increasing array pitch is clearly visible. This absorption band can be attributed to pitch-dependent collective surface plasmon polariton (SPP) resonance modes that are excited when incident light interacts with the hexagonal lattice of ND arrays. The resonance condition can be expressed as 44

$$p = \sqrt{\frac{4}{3}(m^2 + mn + n^2)}\lambda_{\text{SPP}}$$
 (2)

where m and n are integers denoting different-order SPP resonances and λ_{SPP} is the surface plasmon wavelength calculated by the finite-difference frequency-domain method in the air/perovskite/gold three-layer system. Both (m = 1, n =0) and (m = 0, n = 1) indicate two degenerate first-order SPPs. The peak shift resulting from collective SPP modes is confirmed by superimposing the first-order SPP dispersion (dashed blue line) on the total absorption spectra, as shown in Figure 3a. Despite small deviations, the positions of the perovskite absorption peaks coincide with those of the total absorption. For incident light of different polarizations, the electric field can be decomposed into two first-order SPP components, and therefore, the spectral shapes are independent of incident polarization (see Supporting Information). In contrast, perovskite absorption in the presence of NH arrays does not exhibit a significant spectral peak shift, as shown in Figure 3b. Indeed, incident light with wavelength shorter than the band gap wavelength is strongly absorbed by the perovskite film, in a single-pass, and therefore, very little light reaches the NHs and can interact with them. Therefore, collective SPP resonances are suppressed. At longer incident wavelengths, the perovskite material becomes almost transparent near its band edge; therefore, the incident light can strongly interact with the NHs beneath, causing significant SPP interference and absorption enhancement. Indeed, a narrow yellow band at the lower right corner of Figure 3b indicates an increase in overall light absorption, which is caused by plasmonic interference effects.

The simulation results imply that different nanostructures may be employed to optimize light absorption for perovskite films with different thicknesses. For thin films lacking Fabry—Pérot cavity modes, nanostructures with stronger plasmon resonances can achieve higher absorption, while for thick films, nanostructures should be designed to preserve the cavity modes in addition to preserving the plasmonic enhancement.

An upper limit for PCE can be estimated for various cell geometries by using the obtained absorption spectra $A_{\text{perov}}(\lambda)$ in MAPbI₃ and performing detailed balance calculations as follows

$$PCE = \frac{\int_{\lambda < \lambda_{g}} \frac{dJ_{\gamma}}{d\lambda} \frac{\lambda}{2\pi\hbar c} A_{perov}(\lambda) E_{g} d\lambda}{1 \text{ sun}}$$
(3)

where $\mathrm{d}J_\gamma/\mathrm{d}\lambda$ is the AM1.5 G solar spectrum, 46 \hbar is the reduced Planck constant, c is the speed of light in vacuum, λ is the incident wavelength, λ_g is the wavelength corresponding to the perovskite energy band gap (E_g) , and 1 sun is the incident solar power density of 1000 W/m². It is worth pointing out that, with the detailed balance assumption, the obtained values of PCE represent an ideal upper limit for the simulated solar cells. Practically, the PCE of a thicker-film cell is lower than that of a thinner one with same absorption because of its relatively lower V_OC . Therefore, the PCE of a thicker cell is overestimated compared with that of a thin-film cell.

In order to optimize the geometry for different perovskite thicknesses, parameters over a broad range are investigated, that is, D = 50-200 nm with a step of 25 nm, p = 200-350 nmwith a step of 50 nm, and $h = \pm 40$ and ± 70 nm. Representative PCE values are shown in Figure 4 for $h = \pm 70$ nm with t = 400, 150, and 100 nm. For t = 400 nm, the PCE values do not depend significantly on nanostructure dimensions. This results from strong single-pass light absorption in the thick perovskite film, which prevents light from reaching the nanostructure with consequent suppression of plasmonic enhancement. However, for thinner active layers (i.e., t = 150 and 100 nm), plasmonic enhancement becomes more significant for certain nanostructures. For t = 150 nm, higher PCE values can be achieved with arrays of NHs because they can better preserve the Fabry-Pérot cavity modes, compared to ND arrays that show higher scattering cross section. On the contrary, for t = 100 nm, NDs generally show better performance than NHs for various pitches and diameters, while both NDs and NHs yield a maximum PCE of 29.1 and 29.2%, respectively. This enhancement mostly results from plasmonic effects. The PCE values of optimized structures as a function of perovskite film thickness t are shown in Figure 5, together with reference values for flat cases (dashed gray line). The PCE for a flat film oscillates, showing maxima at t = 186 and 338 nm corresponding to PCE = 30 and 31.3%, respectively. The oscillation results from constructive and destructive interference effects within the perovskite film. The blue and red symbols correspond to optimized PCE values in the presence of NHs and NDs, respectively, whereas (p, h, D) denotes the geometric parameters for optimized structures that show maximum PCE, for any given perovskite thickness. Generally, both NH and ND structures yield a similar PCE at wavelengths near the flat cell PCE minima (where there is constructive interference), while at other wavelengths (where there is destructive interference), NHs generally yield higher PCE. By employing proper nanostructures, the PCE for a 100

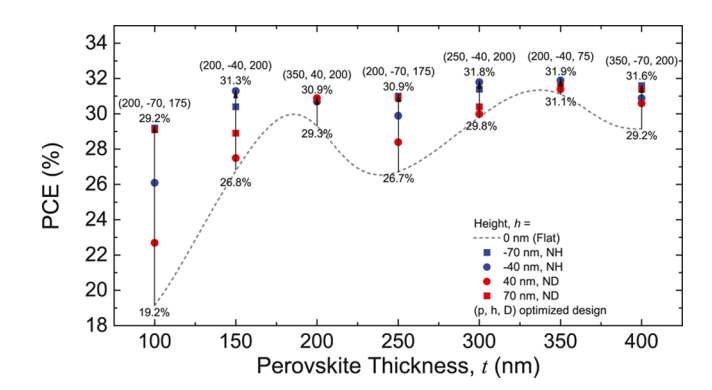


Figure 5. Maximum PCE achievable in optimized ND (blue symbols)/NH (red symbols) arrays as a function of perovskite film thickness, for $h=\pm 40$ (circle symbols) and ± 70 nm (square symbols). The dashed gray line represents the PCE of flat structures. The values in parentheses denote the geometry parameters (p, h, D) that give rise to maximum PCE. A strong PCE enhancement is clearly observed in the presence of plasmonic arrays.

nm-thick cell can be increased from 19.2 to 29.2%, comparable to that of a 400 nm-thick flat cell.

CONCLUSIONS

We reported on a systematic simulation study aimed at enhancing the performance of perovskite solar cells by employing two common plasmonic structures consisting of ND or NH arrays on the back metal contact. We show that plasmonic effects such as plasmon resonances in nanostructures and interference between propagating SPPs supported by the corrugated metal film, together with Fabry-Pérot cavity modes existing within the thin perovskite film, play an essential role in enhancing light absorption of the active perovskite material. We found that opportunely designed metal nanostructures can significantly improve the absorption efficiency and showed that a cell with a 100 nm-thick perovskite film can have PCE comparable to thick, bulk-like cells. The findings reported here may offer an important guideline for the fabrication of plasmon-enhanced highperformance solar cells that employ ultrathin perovskite films.

ASSOCIATED CONTENT

Supporting Information

The Supporting Information is available free of charge on the ACS Publications website at DOI: 10.1021/acs.jpcc.8b07063.

Refractive indices of MAPbI₃ and gold; light propagation depth in MAPbI₃; absorption in gold and total absorption spectra; and polarization-independent absorption spectra (PDF)

AUTHOR INFORMATION

Corresponding Author

*E-mail: Domenico Pacifici@brown.edu.

ORCID ®

Tianyi Shen: 0000-0001-9228-9478

Notes

The authors declare no competing financial interest.

ACKNOWLEDGMENTS

This research was supported by the National Science Foundation under grant no. OIA-1538893. The authors

thank Dingdong Li, Dongfang Li, Nitin Padture, and Yuanyuan Zhou for fruitful discussions. This research was partly conducted using computational resources and services at the Center for Computation and Visualization, Brown University.

REFERENCES

- (1) Jeon, N. J.; Na, H.; Jung, E. H.; Yang, T.-Y.; Lee, Y. G.; Kim, G.; Shin, H.-W.; Seok, S. I.; Lee, J.; Seo, J. A fluorene-terminated hole-transporting material for highly efficient and stable perovskite solar cells. *Nat. Energy* **2018**, *3*, 682–689.
- (2) Yang, S.; Fu, W.; Zhang, Z.; Chen, H.; Li, C.-Z. Recent advances in perovskite solar cells: efficiency, stability and lead-free perovskite. *J. Mater. Chem. A* **2017**, *5*, 11462–11482.
- (3) Elumalai, N.; Mahmud, M.; Wang, D.; Uddin, A. Perovskite solar cells: progress and advancements. *Energies* **2016**, *9*, 861.
- (4) Chen, M.; Ju, M.-G.; Carl, A. D.; Zong, Y.; Grimm, R. L.; Gu, J.; Zeng, X. C.; Zhou, Y.; Padture, N. P. Cesium titanium (IV) bromide thin films based stable lead-free perovskite solar cells. *Joule* **2018**, 2, 558–570.
- (5) Song, Z.; Watthage, S. C.; Phillips, A. B.; Heben, M. J. Pathways toward high-performance perovskite solar cells: review of recent advances in organo-metal halide perovskites for photovoltaic applications. *J. Photonics Energy* **2016**, *6*, 022001.
- (6) Zhou, Y.; Zhou, Z.; Chen, M.; Zong, Y.; Huang, J.; Pang, S.; Padture, N. P. Doping and alloying for improved perovskite solar cells. *J. Mater. Chem. A* **2016**, *4*, 17623–17635.
- (7) Green, M. A.; Ho-Baillie, A.; Snaith, H. J. The emergence of perovskite solar cells. *Nat. Photonics* **2014**, *8*, 506–514.
- (8) Huang, J.; Yuan, Y.; Shao, Y.; Yan, Y. Understanding the physical properties of hybrid perovskites for photovoltaic applications. *Nat. Rev. Mater.* **2017**, *2*, 17042.
- (9) Dong, Q.; Fang, Y.; Shao, Y.; Mulligan, P.; Qiu, J.; Cao, L.; Huang, J. Electron-hole diffusion lengths> 175 μm in solution-grown CH₁NH₁PbI₁ single crystals. *Science* **2015**, 347, 967–970.
- (10) Kim, H.-S.; Lee, C.-R.; Im, J.-H.; Lee, K.-B.; Moehl, T.; Marchioro, A.; Moon, S.-J.; Humphry-Baker, R.; Yum, J.-H.; Moser, J. E.; et al. Lead iodide perovskite sensitized all-solid-state submicron thin film mesoscopic solar cell with efficiency exceeding 9%. *Sci. Rep.* **2012**, *2*, 591.
- (11) Shockley, W.; Queisser, H. J. Detailed balance limit of efficiency of p-n junction solar cells. *J. Appl. Phys.* **1961**, *32*, 510–519.
- (12) Green, M. A. Limiting photovoltaic efficiency under new ASTM International G173-based reference spectra. *Prog. Photovoltaics* **2012**, 20, 954–959.
- (13) Ogomi, Y.; Morita, A.; Tsukamoto, S.; Saitho, T.; Fujikawa, N.; Shen, Q.; Toyoda, T.; Yoshino, K.; Pandey, S. S.; Ma, T.; et al. CH₃NH₃Sn_xPb_(1-x)I₃ Perovskite solar cells covering up to 1060 nm. *J. Phys. Chem. Lett.* **2014**, *5*, 1004–1011.
- (14) Zong, Y.; Wang, N.; Zhang, L.; Ju, M.-G.; Zeng, X. C.; Sun, X. W.; Zhou, Y.; Padture, N. P. Homogenous Alloys of Formamidinium Lead Triiodide and Cesium Tin Triiodide for Efficient Ideal-Bandgap Perovskite Solar Cells. *Angew. Chem., Int. Ed.* **2017**, *56*, 12658–12662.
- (15) Xiao, Z.; Zhou, Y.; Hosono, H.; Kamiya, T.; Padture, N. P. Bandgap Optimization of Perovskite Semiconductors for Photovoltaic Applications. *Chem.—Eur. J.* **2017**, *24*, 2305.
- (16) Anaya, M.; Lozano, G.; Calvo, M. E.; Míguez, H. ABX₃ Perovskites for Tandem Solar Cells. *Joule* **2017**, *1*, 769.
- (17) Atwater, H. A.; Polman, A. Plasmonics for improved photovoltaic devices. *Nat. Mater.* **2010**, *9*, 205–213.
- (18) Polman, A.; Atwater, H. A. Photonic design principles for ultrahigh-efficiency photovoltaics. *Nat. Mater.* **2012**, *11*, 174–177.
- (19) Gan, Q.; Bartoli, F. J.; Kafafi, Z. H. Plasmonic-enhanced organic photovoltaics: Breaking the 10% efficiency barrier. *Adv. Mater.* **2013**, 25, 2385–2396.
- (20) Yang, J.; You, J.; Chen, C.-C.; Hsu, W.-C.; Tan, H.-r.; Zhang, X. W.; Hong, Z.; Yang, Y. Plasmonic polymer tandem solar cell. *ACS Nano* **2011**, *5*, 6210–6217.

- (21) Ding, I.-K.; Zhu, J.; Cai, W.; Moon, S.-J.; Cai, N.; Wang, P.; Zakeeruddin, S. M.; Grätzel, M.; Brongersma, M. L.; Cui, Y.; et al. Plasmonic dye-sensitized solar cells. *Adv. Energy Mater.* **2011**, *1*, 52–57
- (22) Spinelli, P.; Ferry, V. E.; van de Groep, J.; van Lare, M.; Verschuuren, M. A.; Schropp, R. E. I.; Atwater, H. A.; Polman, A. Plasmonic light trapping in thin-film Si solar cells. *J. Opt.* **2012**, *14*, 024002.
- (23) Ferry, V. E.; Verschuuren, M. A.; Li, H. B. T.; Verhagen, E.; Walters, R. J.; Schropp, R. E. I.; Atwater, H. A.; Polman, A. Light trapping in ultrathin plasmonic solar cells. *Opt. Express* **2010**, *18*, A237—A245.
- (24) Zhu, J.; Hsu, C.-M.; Yu, Z.; Fan, S.; Cui, Y. Nanodome solar cells with efficient light management and self-cleaning. *Nano Lett.* **2010**, *10*, 1979–1984.
- (25) Nakayama, K.; Tanabe, K.; Atwater, H. A. Plasmonic nanoparticle enhanced light absorption in GaAs solar cells. *Appl. Phys. Lett.* **2008**, 93, 121904.
- (26) Jiménez-Solano, A.; Carretero-Palacios, S.; Míguez, H. Absorption enhancement in methylammonium lead iodide perovskite solar cells with embedded arrays of dielectric particles. *Opt. Express* **2018**, *26*, A865–A878.
- (27) Miranda-Muñoz, J. M.; Carretero-Palacios, S.; Jiménez-Solano, A.; Li, Y.; Lozano, G.; Míguez, H. Efficient bifacial dye-sensitized solar cells through disorder by design. *J. Mater. Chem. A* **2016**, *4*, 1953–1961.
- (28) Carretero-Palacios, S.; Jiménez-Solano, A.; Míguez, H. Plasmonic nanoparticles as light-harvesting enhancers in perovskite solar cells: a user's guide. ACS Energy Lett. 2016, 1, 323–331.
- (29) Carretero-Palacios, S.; Calvo, M. E.; Míguez, H. Absorption enhancement in organic–inorganic halide perovskite films with embedded plasmonic gold nanoparticles. *J. Phys. Chem. C* **2015**, *119*, 18635–18640.
- (30) Kang, S. M.; Jang, S.; Lee, J.-K.; Yoon, J.; Yoo, D.-E.; Lee, J.-W.; Choi, M.; Park, N.-G. Moth-Eye TiO_2 Layer for Improving Light Harvesting Efficiency in Perovskite Solar Cells. *Small* **2016**, *12*, 2443–2449.
- (31) Mali, S. S.; Shim, C. S.; Kim, H.; Patil, P. S.; Hong, C. K. In situ processed gold nanoparticle-embedded TiO₂ nanofibers enabling plasmonic perovskite solar cells to exceed 14% conversion efficiency. *Nanoscale* **2016**, *8*, 2664–2677.
- (32) Saliba, M.; Zhang, W.; Burlakov, V. M.; Stranks, S. D.; Sun, Y.; Ball, J. M.; Johnston, M. B.; Goriely, A.; Wiesner, U.; Snaith, H. J. Plasmonic-Induced Photon Recycling in Metal Halide Perovskite Solar Cells. *Adv. Funct. Mater.* **2015**, 25, 5038–5046.
- (33) Lu, Z.; Pan, X.; Ma, Y.; Li, Y.; Zheng, L.; Zhang, D.; Xu, Q.; Chen, Z.; Wang, S.; Qu, B.; et al. Plasmonic-enhanced perovskite solar cells using alloy popcorn nanoparticles. *RSC Adv.* **2015**, *5*, 11175–11179.
- (34) Zhang, W.; Saliba, M.; Stranks, S. D.; Sun, Y.; Shi, X.; Wiesner, U.; Snaith, H. J. Enhancement of perovskite-based solar cells employing core—shell metal nanoparticles. *Nano Lett.* **2013**, *13*, 4505–4510.
- (35) Mao, J.; Sha, W. E. I.; Zhang, H.; Ren, X.; Zhuang, J.; Roy, V. A. L.; Wong, K. S.; Choy, W. C. H. Novel direct nanopatterning approach to fabricate periodically nanostructured perovskite for optoelectronic applications. *Adv. Funct. Mater.* **2017**, *27*, 1606525.
- (36) Wang, H.; Haroldson, R.; Balachandran, B.; Zakhidov, A.; Sohal, S.; Chan, J. Y.; Zakhidov, A.; Hu, W. Nanoimprinted perovskite nanograting photodetector with improved efficiency. *ACS Nano* **2016**, *10*, 10921–10928.
- (37) Long, M.; Chen, Z.; Zhang, T.; Xiao, Y.; Zeng, X.; Chen, J.; Yan, K.; Xu, J. Ultrathin efficient perovskite solar cells employing a periodic structure of a composite hole conductor for elevated plasmonic light harvesting and hole collection. *Nanoscale* **2016**, *8*, 6290–6299.
- (38) Paetzold, U. W.; Qiu, W.; Finger, F.; Poortmans, J.; Cheyns, D. Nanophotonic front electrodes for perovskite solar cells. *Appl. Phys. Lett.* **2015**, *106*, 173101.

- (39) Taur, Y.; Ning, T. H. Fundamentals of Modern VLSI Devices; Cambridge University Press: Cambridge, U.K., 2013.
- (40) Maniarasu, S.; Manjunath, V.; Veerappan, G.; Ramasamy, E. Flexible Perovskite Solar Cells. *Perovskite Photovoltaics*; Academic Press, 2018; pp 341–371.
- (41) Lumerical Inc. https://www.lumerical.com/tcad-products/fdtd/ (accessed Sept 6, 2018).
- (42) Löper, P.; Stuckelberger, M.; Niesen, B.; Werner, J.; Filipič, M.; Moon, S.-J.; Yum, J.-H.; Topič, M.; De Wolf, S.; Ballif, C. Complex refractive index spectra of CH₃NH₃PbI₃ perovskite thin films determined by spectroscopic ellipsometry and spectrophotometry. *J. Phys. Chem. Lett.* **2014**, *6*, 66–71.
- (43) Haynes, W. M. CRC Handbook of Chemistry and Physics; CRC Press: Boca Raton, Florida, USA, 2014.
- (44) Ekşioğlu, Y.; Cetin, A. E.; Petráček, J. Optical response of plasmonic nanohole arrays: comparison of square and hexagonal lattices. *Plasmonics* **2016**, *11*, 851–856.
- (45) Sha, W. E. I.; Ren, X.; Chen, L.; Choy, W. C. H. The efficiency limit of CH₃NH₃PbI₃ perovskite solar cells. *Appl. Phys. Lett.* **2015**, *106*, 221104.
- (46) NREL Solar Spectra. https://www.nrel.gov/grid/solar-resource/spectra.html (accessed Sept 6, 2018).